

# Investigations of the Rockfall Impacts on the Flexible Protective Barriers under Seismic Loading

Ziwei Ge

China University of Geosciences Beijing

Hongyan Liu (✉ [liuhy610@sohu.com](mailto:liuhy610@sohu.com))

China University of Geosciences Beijing

---

## Research Article

**Keywords:** rockfall, flexible protective barrier, FLAC3D, seismic wave, dynamic behavior

**Posted Date:** July 12th, 2021

**DOI:** <https://doi.org/10.21203/rs.3.rs-652712/v1>

**License:** © ⓘ This work is licensed under a Creative Commons Attribution 4.0 International License.

[Read Full License](#)

---

---

# Investigations of the rockfall impacts on the flexible protective barriers under seismic loading

Ziwei Ge      Hongyan Liu\*

College of Engineering & Technology, China University of Geosciences (Beijing), Beijing 100083, P R China

## Abstract

Rockfall triggered by earthquakes can cause severe infrastructure losses and even fatalities. The flexible protective barrier is an efficient rockfall protection system that has been widely used against rockfall. This study proposed a novel approach to simulate a field test of rockfall impacting the flexible barrier, and the simulation results showed an excellent match with the field test results. Based on this approach, the seismic loading was applied to the numerical model, and four types of seismic loading were adopted, e.g., non-seismic, x-directional seismic, y-directional seismic, and z-directional seismic. This study aims at investigating the dynamic behavior of the flexible protective barrier under different seismic loading during the rockfall impact process. The following findings can be obtained from the simulation results. First of all, the seismic loading can increase the maximum elongation and decrease the final elongation of the flexible protective barrier comparing to non-seismic loading. Second, the largest deformation area of the protective barrier is at the diagonal position when x-directional seismic loading was applied, which is at the vertical bisector position when y-directional and z-directional seismic loading was applied. Third, the maximum elongation of the protective barrier decreased with the increasing seismic wave period. But in general, the amplitude and period of seismic waves have negligible effects on the elongation, maximum normal stress, and maximum shear stress of the flexible protective barrier.

**Keywords:** rockfall, flexible protective barrier, FLAC3D, seismic wave, dynamic behavior

---

\*corresponding author: [liuhy610@sohu.com](mailto:liuhy610@sohu.com)

## 1 Introduction

The earthquake can easily trigger rockfall, which can cause impact damage to people's lives and engineering structures, such as roadways, railways, and buildings (Mignelli et al. 2013; De Biagi et al. 2017; Abu Seif et al. 2019). Other natural hazards, such as ice melting, mudslide, and landslide, always carry high-energy rocks, which can cause impact damage as well (Margreth et al. 2008; Li et al. 2020; Siyou et al. 2020; Zhao et al. 2020). Protective structures, such as flexible protective barrier (Yang et al. 2019; Boulaud et al. 2020), reinforced concrete structures (Kishi et al. 2010), sand cushions (Kawahara et al. 2006), semi-rigid rockfall protection barrier (Miranda et al. 2015), catch fence (Moon et al. 2014), drapery systems (Thoeni et al. 2014) are often installed to reduce or avoid the impact damage of rockfalls. Among all the types of protection, the flexible protective barrier is an efficient rockfall protection system (Yang et al. 2019).

The flexible protective barrier is usually composed of a metallic cable net, structural steel posts, and an energy dissipation structure (Castanon-Jano et al. 2016). It can dissipate the impact energy by large deformation of the system. When the high-energy moving rock impacts the flexible protective barriers, the ring-shaped mesh is first subjected to the impact. Then the impact force will be transmitted to the structural steel posts, and energy dissipation structure. Finally, the impact

---

45 energy will be dissipated by the elastic-plastic deformation of the energy dissipation structure and  
46 the rockfall will be successfully intercepted at last.

47 The impact process includes large deformation, large slip, contact, separation, material damage,  
48 and other complex nonlinear mechanical behaviors. To better understanding the dynamic behavior  
49 of the flexible protective barrier, field tests and numerical simulations are often carried out. The  
50 standard field test method is to release rock blocks at high places, such as high slopes, artificial  
51 buildings, or towers. And then let rock blocks impact the flexible protective barriers. Finally, the  
52 dynamic properties, such as stress, strain, and velocity, will be recorded by high-speed cameras and  
53 sensors. Spadari et al.(2011) studied the relationship between the size effect and impact force of  
54 falling rocks, and proposed a proportional relationship model that can calculate the impact force of  
55 the other size blocks from a single block. Mitrevski et al. (2006) studied the relationship between  
56 the shape of the impactor and its impact force, and the results showed that the impact force of the  
57 conical impactor is the largest.

58 Despite the field test can truly reflect the dynamic characteristics of the dynamic response of  
59 the flexible protective barrier, the limited number of tests cannot fully explain the rockfall-barrier  
60 interaction mechanisms. Therefore, numerical simulation is an approximation method that can  
61 reproduce the actual barrier behavior of the system during rock impact. Up to now, numerical  
62 simulation has become the mainstream way to study the dynamic response of flexible protective  
63 barriers. Either finite element method (FEM) (Escallón et al. 2014; Castanon-Jano et al. 2018) or  
64 discrete element method (DEM)(Thoeni et al. 2014; Zhu et al. 2019; He et al. 2021) method are  
65 developed to simulate the impact process.

66 Currently, the suitable numerical tool calibrated by field test can provide an effective and  
67 reliable solution for analyzing the dynamic behavior of rockfall-barrier interaction systems. First,  
68 the simulation results are compared to the field test results, and the validity of these approaches was  
69 verified. Based on these approaches, other influencing factors of the rockfall-barrier system can be  
70 analyzed (Gentilini et al. 2012), such as the net panel numerical mesh (Castanon-Jano et al. 2018),  
71 loading geometries (Koo et al. 2016; Yu et al. 2021), successive impacts (Dugelas et al. 2019) and  
72 loading positions (Zhao et al. 2020).

73 Even though the extensive studies on the dynamic behavior of the flexible protective barrier,  
74 there is limited understanding of the effect of the seismic wave on the performance of the flexible  
75 protective barrier. Many post-earthquake investigations have shown that the displacement and  
76 inertial force triggered by the earthquake can affect the dynamic behavior, the connection stiffness,  
77 and the strength of the protective structures (Ling et al. 2001; Liu et al. 2017).

78 Most of the available studies on the effect of seismic waves mainly focused on the rigid  
79 protective structure, such as retaining walls. Kloukinas et al. (2015) used theoretical analysis and  
80 shaking table tests to explore the effect of seismic waves on the dynamic response of the cantilever  
81 retaining walls. Wang et al.(2015) concluded that the far or mid-far field seismic waves had a more  
82 significant impact on the reinforced concrete retaining wall than near field seismic waves. Jo et al.  
83 (2017) investigated that input seismic frequency would cause the phase difference between the  
84 retaining wall and the soil, affecting the earth pressure and the dynamic response of the protective  
85 structure. Lin et al. (2017) used FLAC3D numerical tool to study the dynamic response of the  
86 retaining wall, the earth pressure, and the axial stress of the anchor under the horizontal and vertical  
87 acceleration.

88 Earthquakes can also cause displacement and inertial forces in flexible protective barriers (Liu

---

89 et al. 2017). However, both field tests and numerical simulations assume that the flexible protective  
90 barrier is in a static state. The effect of the earthquakes on the flexible protective barrier is not  
91 considered. Therefore, this study used an explicit finite difference program named FLAC3D to  
92 simulate a field test of rockfall impact flexible protective barrier. The simulation results were  
93 consistent with the field test results, which showed that it was available to use this method to  
94 reproduce the dynamic behavior of the rockfall impact flexible protective barrier. Based on this  
95 method, the effect of seismic wave direction, amplitude, and period on the dynamic behavior of the  
96 flexible protective barrier are considered, which can provide a solution for the design of the flexible  
97 protective barrier in an earthquake area.

## 99 **2 Experimental Data**

### 101 **2.1 Field test introduction**

103 The field test was designed and developed by Gotardi and Govoni (2009) in Fonzaso (Belluno,  
104 Italy). Figures 1 (a)(b)(c) show the general view, lateral view, and front view of the experimental  
105 equipment. The field test is adopted a vertical-drop style in which a concrete block was lifted to the  
106 designated position by a crane and then released to impact the center of the protective barrier. The  
107 experiment process and the elongation during the test can be recorded by the laser sensor and camera.

108 The field test carried out five types of protective barriers, whose commercial names were CTR  
109 05/07/B, CTR 10/04/B, CTR 20/04/B, OM CTR 30/04/A, OM CTR 50/07/ A, corresponding to  
110 energy level 500kJ, 1000kJ, 2000kJ, 3000kJ and 5000kJ, respectively. The main difference between  
111 each protective barrier is the type and location of metallic cable net, structural steel posts, energy  
112 dissipation structure. For more details, please refer to the paper (Gottardi and Govoni 2009).

113 This section selected OM CTR 50/07/A (5000kJ) protective barrier for a brief description,  
114 shown in Fig.2. The basic structure of the flexible protective barrier consists of a metallic cable net,  
115 structural steel posts, energy dissipation structure which is the same as the common protective  
116 barrier. The large mesh directly bears the impact, and the small mesh is used to prevent debris. The  
117 protective net is fixed by four steel T-beams (line 1-5, line 2-6, line 3-7, line 4-8), with an angle of  
118  $10^\circ$  to the horizontal. The protective barrier is connected to the slope by 16 supporting ropes (5  
119 connects to 9, 9b, 10 and 10b; 6 connects to 10, 10b, 11 and 11b; 7 connects to 11, 11b, 12 and 12b;  
120 8 connects to 12,12b, 13 and 13b). In addition, two pairs of lower longitudinal ropes are connected  
121 to anchor 14-15b, 14b-15, and four pairs of upper longitudinal ropes are connected to anchor 8-16b,  
122 8-16, 5-17, 5-17b. The supporting ropes are lines 17-8,17b-8 on the left and lines 16-5, 16b-5 on the  
123 right. Figure 3 shows the principle net steel cable ring (left) and the assumed topology for the mesh  
124 adopted in the FLAC3D model (right).

### 126 **2.2 Experimental results**

128 Table 1 illustrates the results of the field test. The results data included block mass  $m$  ,  
129 measured kinetics of the block ( $E_{km}$ ), impact-related time ( $t_m$ ), maximum elongation ( $e_m$ ), final  
130 elongation ( $e_f$ ). The kinetic of the block ( $E_k$ ) was measured by the laser sensor system. The

131 impact-related time is calculated by the number of frames taken by a high-speed camera. The  
 132 measured impact-related time ( $t_m$ ) is evaluated by the time interval and the number of photos taken  
 133 by a high-speed camera, from the first picture in which block touched barrier to the last picture in  
 134 which the rock has finally stopped. The maximum elongation ( $e_m$ ) and final elongation ( $e_f$ ) are  
 135 measured by the high-speed camera as well.

136 The maximum elongation ( $e_m$ ) and final elongation ( $e_f$ ) of all barriers versus the measured  
 137 kinetic energy ( $E_k$ ) are plotted in Fig.4. The dotted line represents the data fitting equation curve.

138 It can be obtained that the maximum elongation ( $e_m$ ) and the final elongation ( $e_f$ ) are positively  
 139 correlated with the measured kinetic energy ( $E_k$ ), and the data is consistent with the fitted curve. A  
 140 somewhat lower value is provided by barrier 2000kJ, a possibility due to its effective collaborating  
 141 interception structure, which may result in a more minor deformation.

142

143 **Table 1** Experimental data measured in the field tests

| Barrier prototypes (max<br>energy level) | Mass<br>(kg) | Impact<br>energy (kJ) | Time<br>(s) | Maximum<br>Elongation (m) | Final Elongation<br>(m) |
|--|--------------|-----------------------|-------------|---------------------------|-------------------------|
| CTR 05/07/B (500kJ)                      | 1610         | 521                   | 0.17        | 2.95                      | 2.6                     |
| CTR 10/04/B (100kJ)                      | 3320         | 1076                  | 0.22        | 3.95                      | 3.9                     |
| CTR 20/04/B (2000kJ)                     | 6855         | 2203                  | 0.32        | 4.3                       | 4.05                    |
| OM CTR 30/04/A (3000kJ)                  | 9560         | 3136                  | 0.3         | 5.35                      | 4.8                     |
| OM CTR 50/07/A (5000kJ)                  | 16200        | 5246                  | 0.32        | 5.6                       | 5.05                    |

144

### 145 **3 Numerical simulation**

146

#### 147 **3.1 Background and theory**

148

149 In this study, an explicit finite difference program called FLAC3D, which can capture the  
 150 complex nonlinear and large deformation mechanical behaviors of the continuous three-dimensional  
 151 medium, is applied to the rockfall impacting flexible protective barrier simulation. In the dynamic  
 152 analysis, FLAC3D provides a dynamic solution approach for analyzing earthquakes and seismicity.

153 This study used dynamic analysis method for calculating, which is based on the explicit finite  
 154 difference scheme. For a dynamic solution, FLAC3D uses real-point masses derived from the actual  
 155 density of zones to solve the full equations of motion. Figure 5 shows a numerical model based on  
 156 a dynamic solution in FLAC3D. The dynamic loading generated at the bottom of the model, and the  
 157 wave propagated in the internal model. In FLAC3D, dynamic loading can be input through  
 158 acceleration, velocity, stress, and external force from the bottom boundary of the model. In a rigid  
 159 model, the speed and displacement are often input, while the flexible structure frequently inputs  
 160 stress.

161 Local damping is added to dissipate the kinetic energy and reduce unnecessary numerical  
 162 vibrations. The magnitude of local damping is proportional to the unbalanced force. Its direction is

163 taken in the direction of attenuation of the block's vibration, rather than the direction of stable motion.  
 164 Local damping only has a damping effect on accelerated motion and does not affect uniform motion,  
 165 but local damping always puts the system an over-damped state.

166 Boundary conditions refer to the field variables on the model boundary, such as stress values,  
 167 displacement values, etc. The modeling boundary of rock mechanics issues should be unbounded  
 168 theoretically, but the numerical method relies on the finite space discrete grids to analyze the issues.  
 169 Therefore, an appropriate boundary must be artificially truncated. This kind of boundary condition  
 170 will produce stress wave reflections on the boundary when analyzing dynamic problems. These  
 171 reflection waves are superimposed on each other in the model and cannot be dissipated. Therefore,  
 172 FLAC3D adopts the viscous boundary to absorb the stress wave reflections, and the boundary is  
 173 forced to remain non-reflective.

174 In this study, due to the characteristics of a flexible barrier, the input seismic loading is stress.  
 175 The value of local damping is set according to the barrier type. In addition, the normal and tangential  
 176 viscous dampers are set up on the boundaries of the model to absorb external incident waves.

177

### 178 3.2 Numerical model

179

180 Figure 6 shows the numerical model of falling blocks and flexible protective barriers. The  
 181 concrete test block is simplified as a sphere with a density of  $2400 \text{ kg} / \text{m}^3$ , which can be calculated  
 182 by  $m / \rho$ . The falling block is located at 33m height above the center of the flexible protective  
 183 barrier, which can be calculated by  $h = v^2 / 2g$ . The size of the protective barrier is 10m×10m.  
 184 The left and right boundaries (x-direction) are fixed, corresponding to that the flexible protective  
 185 barriers are fixed by supporting ropes.

186

### 187 3.3 Numerical simulating parameters

188

189 Table 2 illustrates the input simulating parameters. The appropriate simulating parameters were  
 190 obtained from many repeated trials to consistent with the actual field test. Since the dynamic  
 191 behavior of flexible protective barriers is mainly analyzed, the mechanical and deformation  
 192 properties of the falling blocks can be ignored. Therefore, the elastic module and stiffness of falling  
 193 block are set to  $1e9 \text{ Pa}$ ,  $1e9 \text{ Pa/m}$  by default. The elastic modulus and local damping of each flexible  
 194 protective barrier positively correlate with impact energy, except energy level 2000kJ. According to  
 195 the above analysis of the field test elongation, the flexible protective barrier 2000kJ has relatively  
 196 high rigidity. Therefore, the simulation parameters can be considered reasonable.

197

198 **Table 2** Numerical simulating parameters

|                   |                      |         |      |      |      |       |      |
|-------------------|----------------------|---------|------|------|------|-------|------|
| Energy level (kJ) |                      |         | 500  | 1000 | 2000 | 3000  | 5000 |
| Ball radius(m)    |                      |         | 0.55 | 0.69 | 0.88 | 0.91  | 1.17 |
| Zone              | Elastic Modulus (Pa) | barrier | 5e5  | 5e5  | 8e5  | 7.5e5 | 1e6  |
|                   |                      | block   | 1e9  |      |      |       |      |
| Interface         | Stiffness(Pa/m)      | barrier | 1e10 | 1e11 | 1e11 | 1e11  | 5e12 |
|                   |                      | block   | 1e9  |      |      |       |      |

|               |      |      |     |      |      |
|---------------|------|------|-----|------|------|
| Local damping | 0.55 | 0.68 | 0.8 | 0.75 | 0.78 |
|---------------|------|------|-----|------|------|

199

### 200 3.4 Simulation results and analysis

201

#### 202 3.4.1 Impact process

203

204 Figures 7-9 compare the impact process of the field impact test (column a) and simulation test  
 205 (column b) of barriers 500kJ, barrier 3000kJ, and barrier 5000kJ. Specifically, the field test pictures  
 206 were taken by a high-speed front camera, describing the impact process. First, the elongation of the  
 207 protective barrier gradually increased to the maximum value, and then the value decreased when the  
 208 block bounced back up. Finally, the flexible protective barriers reached the final elongation and  
 209 remained in a stable state.

210 Figures 7(c), 8(c), 9(c) show the time-elongation history curves, as descriptions of the barrier's  
 211 model during the impact simulation. On these plots, the black dots represent the elongation at four  
 212 moments: two before the maximum elongation, one at the maximum elongation, one after the  
 213 maximum elongation.

214 The overall impact process can be satisfactorily reproduced in these numerical simulations.  
 215 The model's deformed shape is essentially similar to the field test pictures, thereby showing that the  
 216 numerical model can successfully reproduce the dynamic behavior of the flexible protective barriers.

217

#### 218 3.4.2 Stress

219

220 Figures 10 (a)~(e) show the time histories of normal stress and tangential stress at the center  
 221 of the flexible protective barriers. On this plot, The black lines represent normal stress, and the red  
 222 lines represent tangential stress. It can be observed that the time-stress history curve experienced  
 223 four important stages. As an illustration, the barrier 500kJ was selected to analyze. First, at the  
 224 beginning of impact (OA stage), the stress had a sudden transition in a short period, and the ratio of  
 225 stress/time is nearly infinity. Then, at the AB stage before 0.15s, the stress did not change and the  
 226 elongation was still increasing rapidly, shown in Fig.7(c). The barrier temporarily lost its ability to  
 227 resist further deformation, which was also known as the yielding process that the barrier gradually  
 228 transformed an elastic state to a plastic state. With the impact progress going on (BC stage), the  
 229 normal and shear stress increased to the maximum value, as well as the elongation. In the last CD  
 230 stage, the stress exhibited the characteristics of small amplitude oscillations at an equilibrium  
 231 position, and lower energy barriers were more violently than the high-level energy barriers.

232 Figure 10(f) compares the maximum normal stress and maximum tangential stress under  
 233 different impact energy. The results show that the maximum value of normal stress is always greater  
 234 than that of tangential stress. Both two types of stress will increase with the impact energy.

235

#### 236 3.4.3 Elongations

237

238 Figure 11(a) shows the barrier elongation of all the barriers versus impact-related time during  
 239 the simulation. It can be observed that at the beginning of the impact process, all the barriers have  
 240 the nearly identical elongation growth rate, that is,  $\sqrt{Ve/Vt}$ .

241 Figure 11(b) shows the relationship between the elongation of the protective barriers and the

---

242 velocities of the falling blocks. The velocity of the falling block is 0 for two times, corresponding  
243 the moments that the flexible protective barriers reach the maximum and final elongation. When the  
244 velocity of the rockfall decreased to about 15m/s, the capability of intercepting rockfall is different  
245 among each barrier. Before this moment, the reduction of each blocks' velocities is nearly the same.  
246 However, after this moment, the reduction of each blocks' velocities became different. For example,  
247 the velocity of rockfall in barrier 500kJ drops sharply to 0 after the velocity of 15m/s, while in  
248 barrier 5000kJ, the velocity drops slowly. Even a plateau period occurs in which the velocity remains  
249 15m/s in barrier 5000kJ. Therefore, it can be inferred that in the initial impact process, the types of  
250 barriers have no significant effect on the deformation of barriers. In the middle impact process, the  
251 capability of intercepting the rockfall of each barrier is different. The higher-energy barriers  
252 correspond to a lower reduction of rockfall velocity.

253 Figure 12 shows the numerical maximum and final elongation of all the barriers versus energy  
254 level during the field test process, corresponding numerical simulation results. The comparisons  
255 show an excellent match between the field test results and the numerical simulation.

#### 256 257 3.4.4 impact-related time

258  
259 The impact-related time refers to the time from the first time when the block touches the  
260 protective barrier to the last time when the block finally stops moving. Figure 13 compares the  
261 relationship between impact-related time and impact energy in the field test (solid line) and  
262 numerical test (dashed line). The time of the field test is estimated by the time interval and the  
263 number of photos taken by a high-speed camera. The measured impact-related time  $t_m$  increases  
264 from 0.17 to 0.39s.

265 In FLAC3D dynamic analysis, a timestep must be used in the oscillating mass-spring system  
266 with a finite difference scheme. Fig.14 shows the one-dimensional mass-spring system. The motion  
267 of the model point with a virtual displacement is governed by the differential equation (1). The  
268 timestep  $\Delta t$  corresponds to a second-order finite difference scheme for Eq.(1) is given by Eq.(2).

$$269 \quad -kx = m \frac{d^2x}{dt^2} \quad (1)$$

$$270 \quad \Delta t = \frac{T}{\pi} \quad (2)$$

271 Where  $k$  denotes the stiffness of the spring;  $x$  denotes the virtual displacement;  $m$  is  
272 mass;  $T$  is the period of the system;  $\Delta t$  is timestep of the system. The timestep  $\Delta t$  represents  
273 the actual time corresponding to one-step numerical simulation calculation. Hence, the simulating  
274 impact time can be estimated by timestep  $\times$  step.

275 The numerical impact time  $t_n$  is from 0.79 to 1.3s, which is much higher than the measured  
276 impact time  $t_m$ , possibly due to the FLAC3D calculation principle. The basic calculating unit is  
277 called zone in FLAC3D, so the unbalance of any zone may lead to the unbalance of the overall  
278 system. Therefore, it takes a relatively long time to reach the equilibrium state. However, in the field

---

279 test, the impact-related time can be estimated roughly by observing the block stops.

280 In conclusion, It can be observed that the impact process, the elongation of the numerical  
281 simulation results have a remarkable excellent agreement with the field tests results. So far, the  
282 validity of this numerical simulation method has been verified.

## 284 **4 Impact of the seismic wave**

### 286 **4.1 Numerical model**

287  
288 To study the effect of seismic waves on rockfall impact flexible protective barrier, a simple  
289 sine wave loading is selected for simulation analysis. The equation of the sin wave is  
290  $y = A \sin(2\pi t / T)$ , where  $A$  denotes the amplitude of the seismic wave,  $t$  denotes the impact-  
291 related time, and  $T$  denotes the seismic wave period. The sine wave is input as a stress loading at  
292 the bottom of the flexible protective barrier in FLAC3D, and the boundary is a free-field boundary,  
293 as shown in Fig.15. As mentioned in the previous section, the impact-related time of the falling rock  
294 is 0.79~1.3s. Therefore, the maximum period of the sine wave should be less than 0.7s to ensure  
295 that there is at least one complete seismic wave loading during the impact process. In this section,  
296 the period and the amplitude are set to 0.02s/100, respectively. The sine seismic wave is  
297  $y = 100 \sin(\pi t / 0.01)$ . In addition, x-direction, y-direction, and z-direction three directions seismic  
298 wave was carried out to analyze the difference in impact process, elongation, and stress, respectively.

### 300 **4.2 Simulation results and analysis**

#### 302 **4.2.1 Impact process**

303  
304 As an illustration, Figure 16 shows the z-velocity contour of the barrier 500kJ rockfall  
305 impacting the flexible protective barrier, since the vertical deformation is mainly concerned.  
306 Column (a)~(d) are corresponding non-seismic wave loading, x-directional loading, y-directional  
307 loading and z-directional loading, after this referred to as case1~4. The first to fourth rows  
308 correspond to rockfall velocities of 20m/s, 14m/s, 0m/s, 0.7m/s (the velocity direction of the first to  
309 third rows is the negative direction of the z-axis and the fourth row is the positive direction of the  
310 z-axis). These four rows correspond to contact-brake-stationary-rebound four stages of rockfall  
311 impact the flexible protective barrier, after this referred to as stage 1-4. The dynamic response  
312 process of all types of the barrier has similarities and differences. The four stages are described as  
313 follows.

314 Stage 1 is the initial contact stage of the falling rock impacting the flexible protective barrier.  
315 The area around the contact position of the barrier is deformed downwards, and the outer area of  
316 the contact is deformed upwards. As the falling rock continues to fall, the middle falling area  
317 expands in a circle. For the convenience of description, the red, orange, green velocity contour area  
318 with positive velocities are referred to as “up area,” and the blue area with negative velocities are  
319 referred to as “falling area.”

320 Stage 2 is the braking stage of the falling rock. Most of the flexible protective barrier area  
321 belongs to the “falling area.” As the impact process progresses, the “falling area” decreases, and the  
322 “up area” increases until the falling block stops.

---

323 Stage 3 is the stage of block stops. At this stage, the “up area” occupies the main part.

324 Stage 4 is the finally rebound stage. The “falling area” reflects the deformation process of the  
325 flexible protective barrier. The flexible protective barrier is elastically deformed due to the impact  
326 of falling rocks, which makes the inside elastic energy of the flexible protective barrier. The “up  
327 area” is the buffering process of the flexible protective barrier. The elastic energy of the flexible  
328 protective barrier is converted into kinetic energy to provide upward force for falling rock to stop  
329 the falling rock.

330 The main difference in the dynamic response of the flexible protective barrier under four cases  
331 is the different shape of the velocity contour, specifically described as follows.

332 At stage 2, the velocity contours of case 1 and case 2-4 are different. The velocity contour of  
333 case 2 and 4 are similar: the velocity contour in the “falling area” is X-shaped distribution, and the  
334 “falling area” internal velocity is greater than the edge velocity. It indicates that the most significant  
335 deformation of cases 2 and 4 is at the diagonal of the flexible protective barrier. The velocity contour  
336 of case 1 is approximately orthogonal “+” shaped. It indicates that the largest deformation of the  
337 case1 is at the vertical bisector of the flexible protective barrier.

338 At stage 3, the four cases show apparent differences. The “falling area” of case 1 is  
339 concentrated in the middle part and distributed in strips. The “up area” of case 2 is roughly  
340 distributed in an X-shape. Combined stage 3 with stage 2, the “up area” and the “falling area” appear  
341 alternately, but concentrate in the diagonal area of the flexible protective barrier, which can infer  
342 that this area is reciprocating up and down. Due to the result analysis, the strength and deformation  
343 of the diagonal area of the flexible protective barrier should be paid more attention to in case 2. The  
344 “up area” of case 3 is concentrated on the horizontal centerline of the flexible protective barrier, and  
345 the “falling zone” is distributed at the upper and lower boundaries of the flexible protective barrier.  
346 In case 3, the “falling area” is concentrated on the horizontal centerline of the flexible protective  
347 barrier, and the “up area” is distributed on the upper and lower boundaries of the flexible protective  
348 barrier.

349 In stage 3, the “up area” of case 1 is roughly distributed in a circle shape and X-shape in case  
350 2, vertical strips in case 3, X-to-stripes shape in case 4.

351 Therefore, the most considerable deformation area is the vertical bisector of the flexible  
352 protective barrier, when there is non-seismic wave loading. The main buffering area is the  
353 circumferential range of the falling rock in non-seismic wave loading case. When the x-directional  
354 seismic wave is loaded, the most considerable deformation area is at the diagonal intersection of the  
355 flexible protective barrier. The main buffering area is on the opposite corner of the flexible  
356 protective barrier. When the y-direction or z-direction seismic wave is loaded, the most significant  
357 deformation is at the horizontal and vertical cross line.

358

#### 359 4.2.2 Seismic loading direction

360

361 Figure 17 shows the comparison between the maximum elongation and the final elongation of  
362 the barrier center in cases 2-4. The hollow icons represent the maximum elongation, and the solid  
363 icons represent the final elongation. For the maximum elongation, the three directions seismic wave  
364 can increase the elongation as well. The maximum elongation of z-directional seismic waves loading  
365 increases most at low energy levels (500kJ,100kJ). With the rise of impact energy, the three types  
366 of seismic waves have more minor differences. For the final elongation, the loading of the seismic

---

367 wave will reduce the final elongation, and the x-directional seismic wave reduce most obviously.

368

#### 369 4.2.3 Seismic wave period

370

371 The seismic wave period can cause the vibration phase difference between the flexible  
372 protective barrier and the falling rock. In the rock impacting the flexible protective barrier, the  
373 interaction between the flexible protective barrier and the falling rock may be in the same or  
374 different phase during the seismic wave loading process. The phase will affect the dynamic response  
375 of the flexible protective barrier.

376 To investigate the influence of the seismic wave period, the cases of periods 0.02s, 0.04s, 0.1s,  
377 0.2s are selected to study. Figure 18 shows the relationship between the maximum elongation, the  
378 maximum shear stress, the maximum normal stress, and the seismic wave period. The seismic wave  
379 direction is z-direction. It can be seen that as the period increases, the maximum elongation  
380 decreases. The seismic wave period affects minor on the maximum normal and tangential.

381

#### 382 4.2.4 Seismic wave amplitude

383

384 To investigate the influence of the seismic wave amplitude, the cases of amplitudes 10, 50, 100,  
385 500, and 1000 are simulated, respectively. Figure 19 shows the relationship between the maximum  
386 elongation, normal stress, and tangential stress of x-directional, y-directional and z-directional  
387 seismic wave loading. The results show that the maximum elongation of the z-directional seismic  
388 wave is affected more than the other two directions. As the seismic wave amplitude increases, the  
389 maximum elongation decreases. The amplitude has minor effect on the maximum normal stress, and  
390 shear stress in all three directions.

391

## 392 5 Conclusion

393

394 This paper used FLAC3D to simulate a field test and study the dynamic response of the rockfall  
395 impact flexible protective barrier under seismic loading. The effect of seismic wave direction, period,  
396 amplitude on the maximum elongation, final elongation, maximum normal stress, and maximum  
397 shear stress are analyzed. The following conclusions are obtained.

398 (1) Comparing with the non-seismic action, the maximum elongation, normal stress, shear  
399 stress increases, and the final elongation decreases with seismic wave action. Therefore, the tensile  
400 and shear strength of the designed flexible protective barrier considering the seismic effect should  
401 be greater than that of the non-seismic action.

402 (2) In the initial impact process, the types of the barriers have negligible effects on the  
403 deformation of the barriers. In the middle impact process, the capability of intercepting rockfall of  
404 each barrier is different, in which the higher-energy barriers correspond to a lower reduction of  
405 rockfall velocity.

406 (3) From the analysis of the seismic wave dynamic response velocity contour, it can be seen  
407 that the main deformation area of the flexible protective barrier under the x-directional seismic wave  
408 is the diagonal of the flexible protective barrier. The main deformation area of the flexible protective  
409 barrier under the y-directional and z-directional seismic wave is the vertical bisector of the flexible  
410 protective barrier. Therefore, the strength at the diagonal area of the flexible protective barrier

---

411 should be strengthened under the x-directional seismic wave. The strength at the vertical bisector  
412 area of the flexible protective barrier should be strengthened under the y-directional and z-  
413 directional seismic waves.

414 (4) The maximum elongation decreases with the increasing seismic wave period. But in  
415 general, the period has little effect on the elongation and stress of the flexible protective barrier,  
416 neither does the seismic wave amplitude.

417

## 418 **References**

419 Abu Seif E-SS, Bahabri AA (2019) Rockfall hazards assessment along the Aswan–Cairo highway, Sohag  
420 Governorate, Upper Egypt. *Nat Hazards* 99: 991-1005. <http://doi.org/10.1007/s11069-019-03788->  
421 [w](http://doi.org/10.1007/s11069-019-03788-w)

422 Boulaud R, Douthe C, Sab K (2020) Modelling of curtain effect in rockfall barrier with the dynamic  
423 relaxation. *Int J Solids Struct* 200-201: 297-312. <http://doi.org/10.1016/j.ijsolstr.2020.01.008>

424 Castanon-Jano L, Blanco-Fernandez E, Castro-Fresno D, Ballester-Muñoz F (2016) Energy Dissipating  
425 Devices in Falling Rock Protection Barriers. *Rock Mech Rock Eng* 50: 603-619.  
426 <http://doi.org/10.1007/s00603-016-1130-x>

427 Castanon-Jano L, Blanco-Fernandez E, Castro-Fresno D, Ferreño D (2018) Use of explicit FEM models  
428 for the structural and parametrical analysis of rockfall protection barriers. *Eng Struct* 166: 212-226.  
429 <http://doi.org/10.1016/j.engstruct.2018.03.064>

430 De Biagi V, Napoli ML, Barbero M (2017) A quantitative approach for the evaluation of rockfall risk on  
431 buildings. *Nat Hazards* 88: 1059-1086. <http://doi.org/10.1007/s11069-017-2906-3>

432 Dugelas L, Coulibaly JB, Bourrier F, Lambert S, Chanut M-A, Olmedo I, Nicot F (2019) Assessment of  
433 the predictive capabilities of discrete element models for flexible rockfall barriers. *Int J Impact Eng*  
434 133: 103365. <http://doi.org/10.1016/j.ijimpeng.2019.103365>

435 Escallón JP, Wendeler C, Chatzi E, Bartelt P (2014) Parameter identification of rockfall protection barrier  
436 components through an inverse formulation. *Eng Struct* 77: 1-16.  
437 <http://doi.org/10.1016/j.engstruct.2014.07.019>

438 Gentilini C, Govoni L, De Miranda S, Gottardi G, Ubertini F (2012) Three-dimensional numerical  
439 modelling of falling rock protection barriers. *Comput Geotech* 44: 58-72.  
440 <http://doi.org/10.1016/j.compgeo.2012.03.011>

441 Gottardi G, Govoni L (2009) Full-scale Modelling of Falling Rock Protection Barriers. *Rock Mech Rock*  
442 *Eng* 43: 261-274. <http://doi.org/10.1007/s00603-009-0046-0>

443 He Y, Nie L, Lv Y, Wang H, Jiang S, Zhao X (2021) The study of rockfall trajectory and kinetic energy  
444 distribution based on numerical simulations. *Nat Hazards* 106: 213-233.  
445 <http://doi.org/10.1007/s11069-020-04457-z>

446 Jo S-B, Ha J-G, Lee J-S, Kim D-S (2017) Evaluation of the seismic earth pressure for inverted T-shape  
447 stiff retaining wall in cohesionless soils via dynamic centrifuge. *Soil Dyn Earthquake Eng* 92: 345-  
448 357. <http://doi.org/10.1016/j.soildyn.2016.10.009>

449 Kawahara S, Muro T (2006) Effects of dry density and thickness of sandy soil on impact response due to  
450 rockfall. *J Terramech* 43: 329-340. <http://doi.org/10.1016/j.jterra.2005.05.009>

451 Kishi N, Bhatti AQ (2010) An equivalent fracture energy concept for nonlinear dynamic response analysis  
452 of prototype RC girders subjected to falling-weight impact loading. *Int J Impact Eng* 37: 103-113.  
453 <http://doi.org/10.1016/j.ijimpeng.2009.07.007>

454 Kloukinas P, Scotto Di Santolo A, Penna A, Dietz M, Evangelista A, Simonelli AL, Taylor C, Mylonakis

---

455 G (2015) Investigation of seismic response of cantilever retaining walls: Limit analysis vs shaking  
456 table testing. *Soil Dyn Earthquake Eng* 77: 432-445. <http://doi.org/10.1016/j.soildyn.2015.05.018>

457 Koo RCH, Kwan JSH, Lam C, Ng CWW, Yiu J, Choi CE, Ng AKL, Ho KKS, Pun WK (2016) Dynamic  
458 response of flexible rockfall barriers under different loading geometries. *Landslides* 14: 905-916.  
459 <http://doi.org/10.1007/s10346-016-0772-9>

460 Li X, Zhao J, Kwan JSH (2020) Assessing debris flow impact on flexible ring net barrier: A coupled CFD-  
461 DEM study. *Comput Geotech* 128: 103850. <http://doi.org/10.1016/j.compgeo.2020.103850>

462 Lin Y-L, Yang G-L, Yang X, Zhao L-H, Shen Q, Qiu M-M (2017) Response of gravity retaining wall with  
463 anchoring frame beam supporting a steep rock slope subjected to earthquake loading. *Soil Dyn*  
464 *Earthquake Eng* 92: 633-649. <http://doi.org/10.1016/j.soildyn.2016.11.002>

465 Ling H, Leshchinsky D, Chouc NNS (2001) post-earthquake investigation on several geosynthetic-  
466 reinforced soil retaining walls and slopes during the Ji-Ji earthquake of Taiwan. *Soil Dyn*  
467 *Earthquake Eng* 21: 297-313. [http://doi.org/10.1016/S0267-7261\(01\)00011-2](http://doi.org/10.1016/S0267-7261(01)00011-2)

468 Liu C, Wei X, Lu Z, Wu H, Yang Y, Chen L (2017) Studies on passive flexible protection to resist  
469 landslides caused by the May 12, 2008, Wenchuan earthquake. *Struct Des Tall Special Build* 26:  
470 e1372. <http://doi.org/10.1002/tal.1372>

471 Margreth S, Roth A (2008) Interaction of flexible rockfall barriers with avalanches and snow pressure.  
472 *Cold Reg Sci Technol* 51: 168-177. <http://doi.org/10.1016/j.coldregions.2007.03.008>

473 Mignelli C, Peila D, Lo Russo S, Ratto SM, Broccolato M (2013) Analysis of rockfall risk on  
474 mountainside roads: evaluation of the effect of protection devices. *Nat Hazards* 73: 23-35.  
475 <http://doi.org/10.1007/s11069-013-0737-4>

476 Miranda S, Gentilini C, Gottardi G, Govoni L, Mentani A, Ubertini F (2015) Virtual testing of existing  
477 semi-rigid rockfall protection barriers. *Eng Struct* 85: 83-94.  
478 <http://doi.org/10.1016/j.engstruct.2014.12.022>

479 Mitrevski T, Marshall IH, Thomson RS, Jones R (2006) Low-velocity impacts on preloaded GFRP  
480 specimens with various impactor shapes. *Compos Struct* 76: 209-217.  
481 <http://doi.org/10.1016/j.compstruct.2006.06.033>

482 Moon T, Oh J, Mun B (2014) Practical design of rockfall catchfence at urban area from a numerical  
483 analysis approach. *Eng Geol* 172: 41-56. <http://doi.org/10.1016/j.enggeo.2014.01.004>

484 Siyou X, Lijun S, Yuanjun J, Xin Q, Min X, Xiaobo H, Zhenyu L (2020) Experimental investigation on  
485 the impact force of the dry granular flow against a flexible barrier. *Landslides* 17: 1465-1483.  
486 <http://doi.org/10.1007/s10346-020-01368-9>

487 Spadari M, Giacomini A, Buzzi O, Hambleton JP (2011) Prediction of the Bullet Effect for Rockfall  
488 Barriers: a Scaling Approach. *Rock Mech Rock Eng* 45: 131-144. <http://doi.org/10.1007/s00603-011-0203-0>

490 Thoeni K, Giacomini A, Lambert C, Sloan SW, Carter JP (2014) A 3D discrete element modelling  
491 approach for rockfall analysis with drapery systems. *Int J Rock Mech Min Sci* 68: 107-119.  
492 <http://doi.org/10.1016/j.ijrmms.2014.02.008>

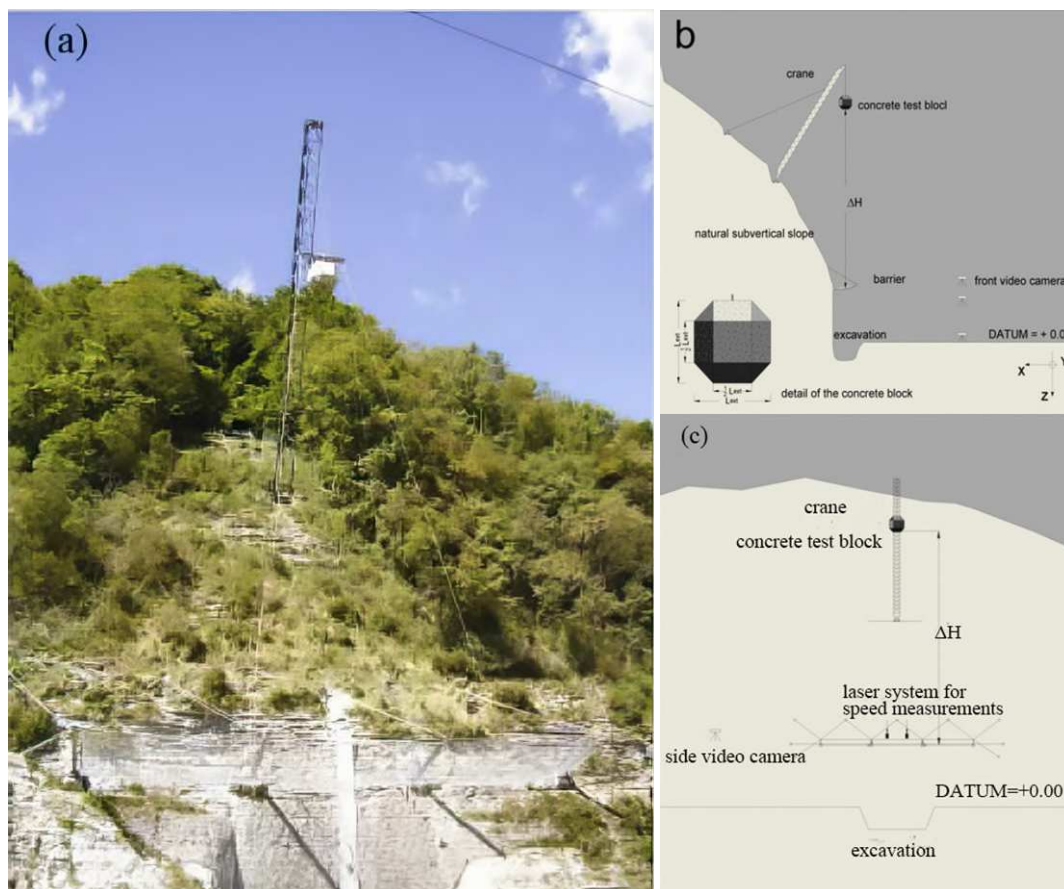
493 Wang L, Chen G, Chen S (2015) Experimental study on seismic response of geogrid reinforced rigid  
494 retaining walls with saturated backfill sand. *Geotext Geomembr* 43: 35-45.  
495 <http://doi.org/10.1016/j.geotextmem.2014.11.006>

496 Yang J, Duan S, Li Q, Liu C (2019) A review of flexible protection in rockfall protection. *Nat Hazards*  
497 99: 71-89. <http://doi.org/10.1007/s11069-019-03709-x>

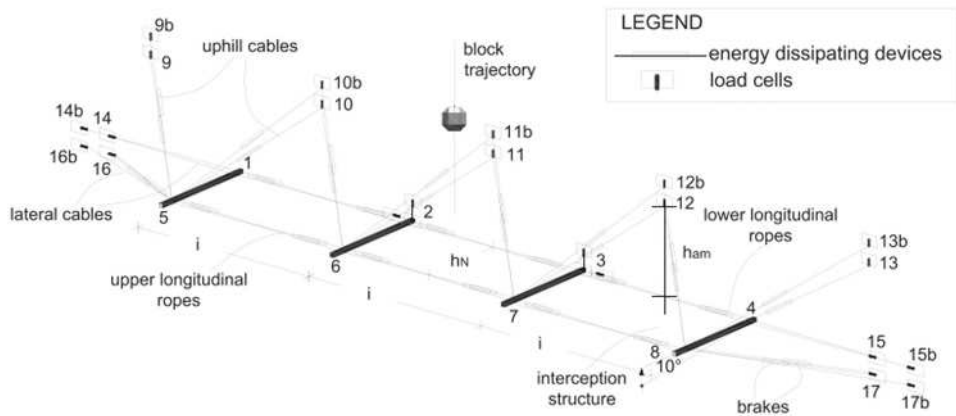
498 Yu Z, Luo L, Liu C, Guo L, Qi X, Zhao L (2021) Dynamic response of flexible rockfall barriers with

499 different block shapes. Landslides 5: 1-17. <http://doi.org/10.1007/s10346-021-01658-w>  
 500 Zhao L, He JW, Yu ZX, Liu YP, Zhou ZH, Chan SL (2020) Coupled numerical simulation of a flexible  
 501 barrier impacted by debris flow with boulders in front. Landslides 17: 2723-2736.  
 502 <http://doi.org/10.1007/s10346-020-01463-x>  
 503 Zhao L, Yu Z-X, Liu Y-P, He J-W, Chan S-L, Zhao S-C (2020) Numerical simulation of responses of  
 504 flexible rockfall barriers under impact loading at different positions. J Constr Steel Res 167: 105953.  
 505 <http://doi.org/10.1016/j.jcsr.2020.105953>  
 506 Zhu Z-H, Yin J-H, Qin J-Q, Tan D-Y (2019) A new discrete element model for simulating a flexible ring  
 507 net barrier under rockfall impact comparing with large-scale physical model test data. Comput  
 508 Geotech 116: 103208. <http://doi.org/10.1016/j.compgeo.2019.103208>

509  
 510 **Figures**

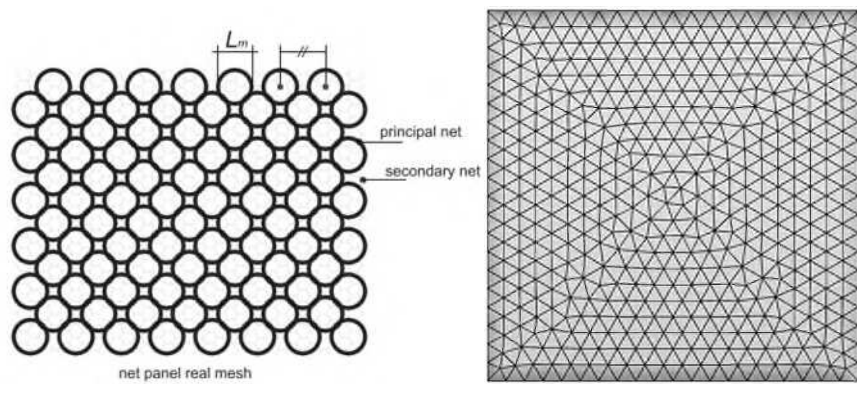


511  
 512 **Fig.1** The field test in Fonzaso (Belluno, Italy): (a) general view, (b) lateral view, (c) front view



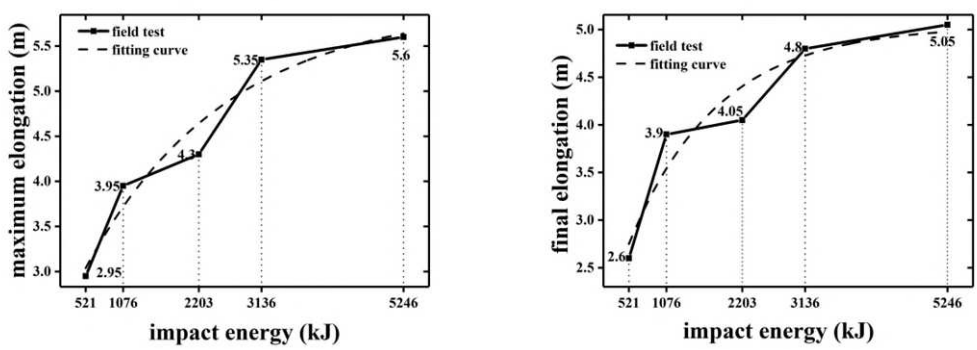
513  
514  
515

**Fig.2** Three-dimensional sketch of the rockfall protective barrier 5000kJ



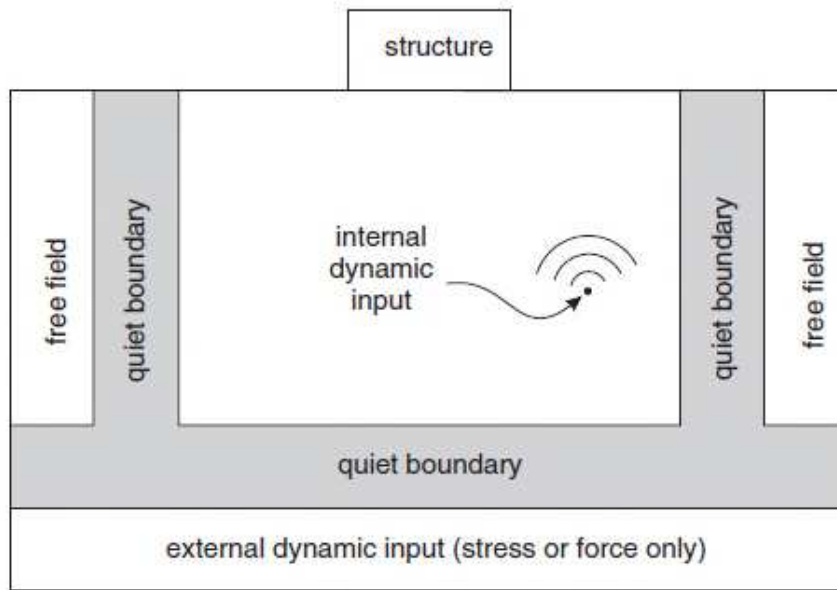
516  
517

**Fig.3** The principle net steel cable ring (left) and the assumed topology FLAC3D model mesh (right)



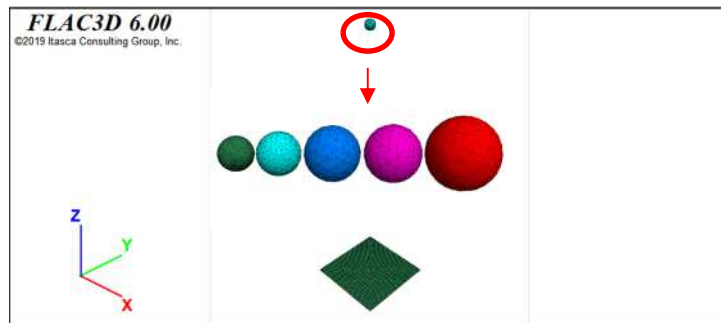
518  
519  
520

**Fig.4** Maximum elongations (left) and final elongations versus impact energy: numerical tests (dotted line) and field tests (solid line)



521

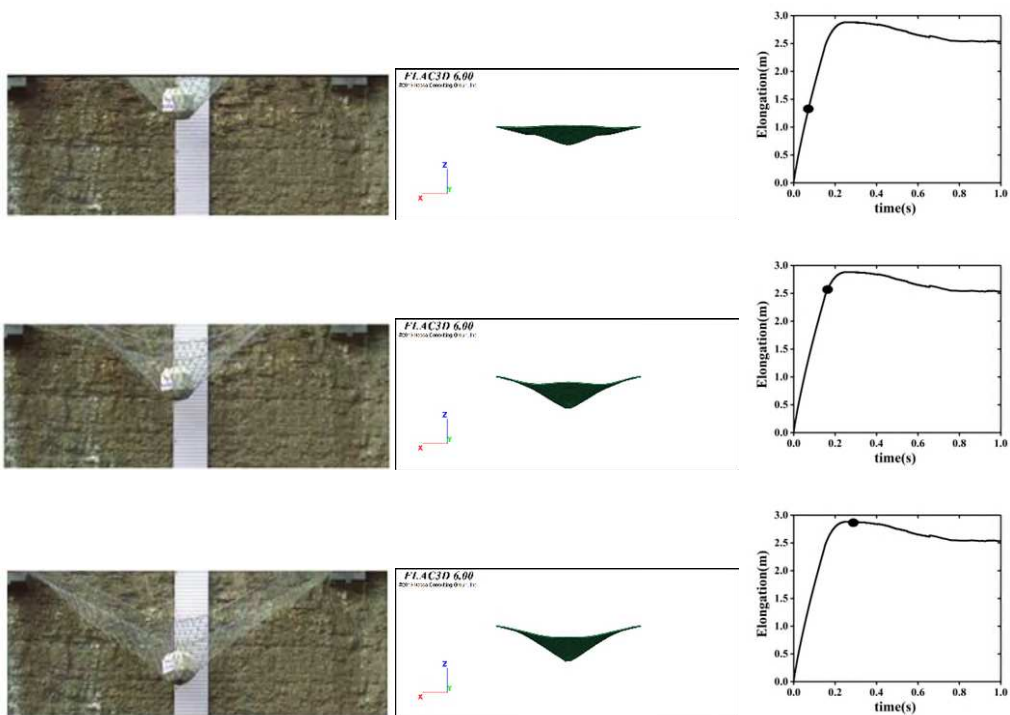
522 **Fig.5** Dynamic loading and boundary conditions available in FLAC3D



523

524 **Fig.6** Numerical models of rockfall and barrier in FLAC3D

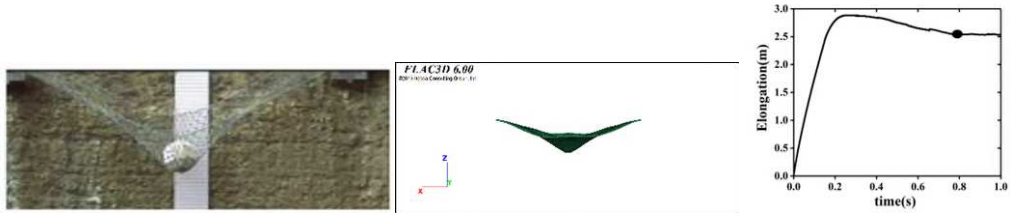
525



526

527

528

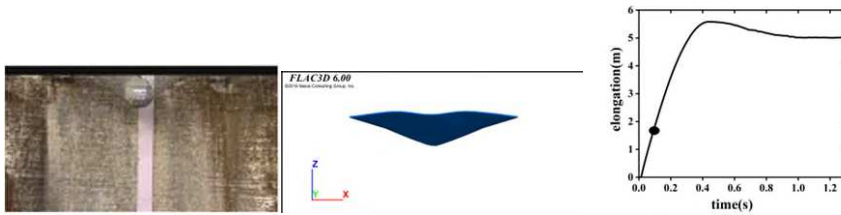


529

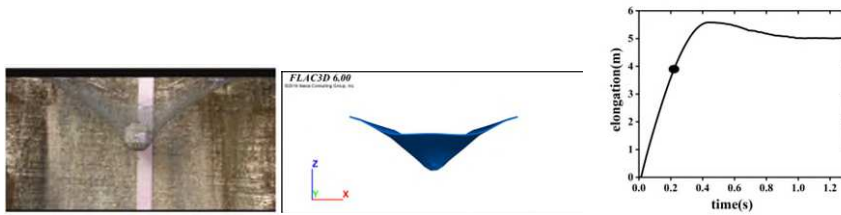
530 **Fig.7** Field test (left) compared with numerical simulation (right) of barrier 500kJ at times  $t_1 =$

531  $0.07s, t_2 = 0.16s, t_3 = 0.28s$  and  $t_4 = 0.79s$

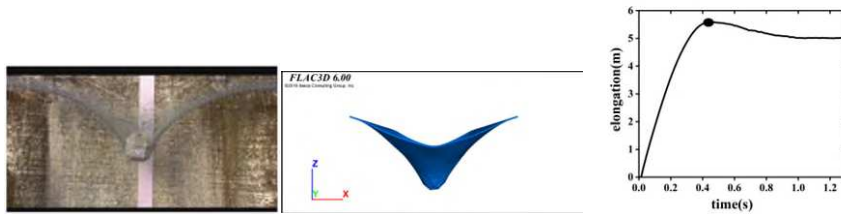
532



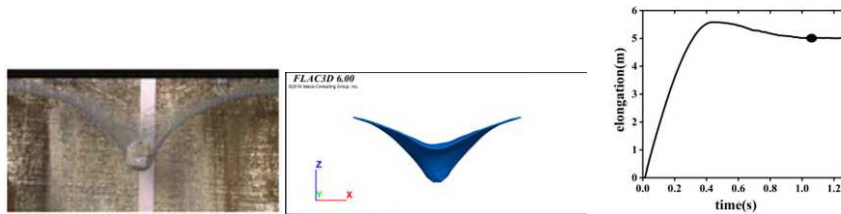
533



534



535

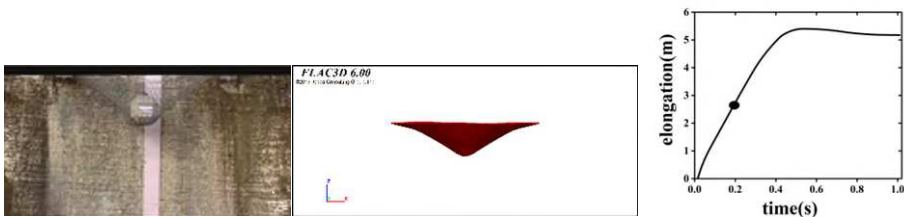


536

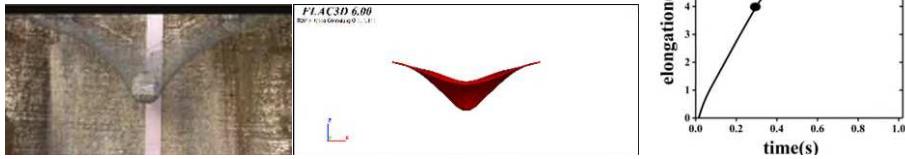
537 **Fig.8** Field test (left) compared with numerical simulation (right) of barrier 3000kJ at times

538  $t_1 = 0.09s, t_2 = 0.22s, t_3 = 0.44s$  and  $t_4 = 1.05s$

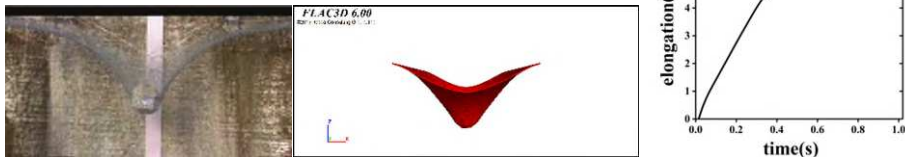
539



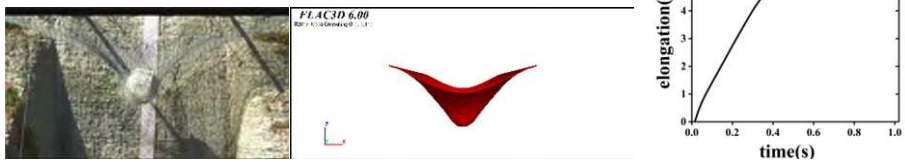
540



541



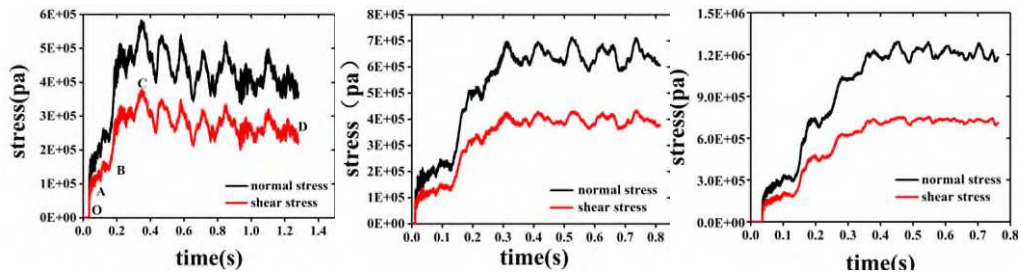
542



543 **Fig.9** Field test (left) compared with numerical simulation (right) of barrier 5000kJ at times  $t_1 =$

544  $0.19s$ ,  $t_2 = 0.3s$ ,  $t_3 = 0.51$  and  $t_4 = 0.94s$

545



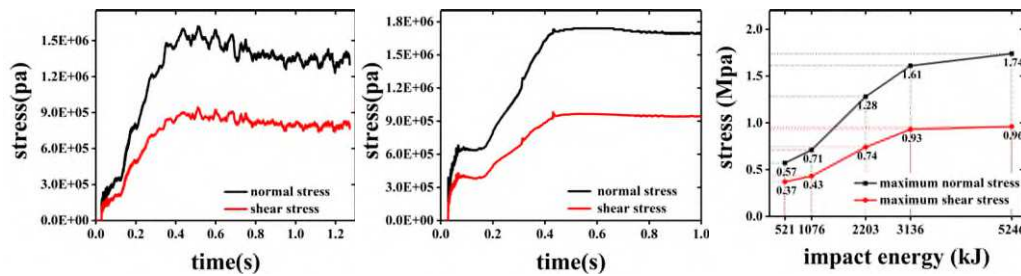
546

(a)

(b)

(c)

547



548

(d)

(e)

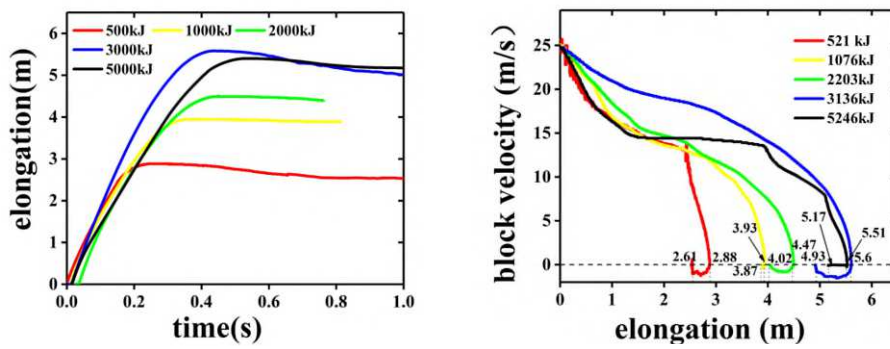
(f)

549

550 **Fig.10** Normal stress (black lines) and shear stress (red lines) versus time (a) barrier 500kJ, (b)

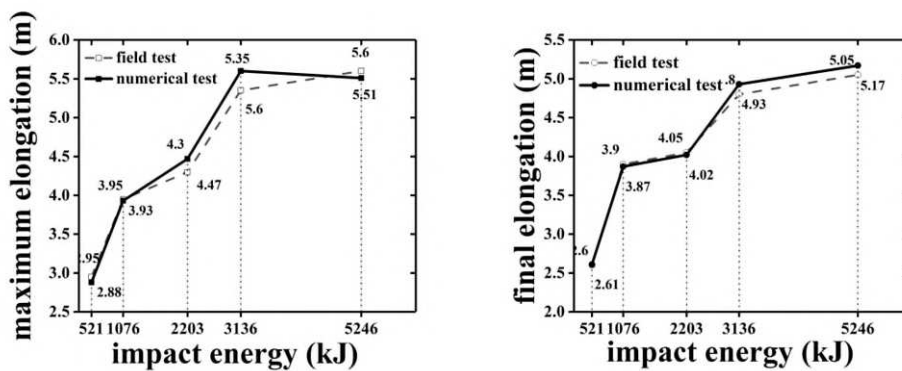
551 barrier 1000kJ, (c) barrier 2000kJ, (d) barrier 3000kJ, (e) barrier 5000kJ, (f) maximum normal stress

552 (black lines) and shear stress (red lines) versus impact energy



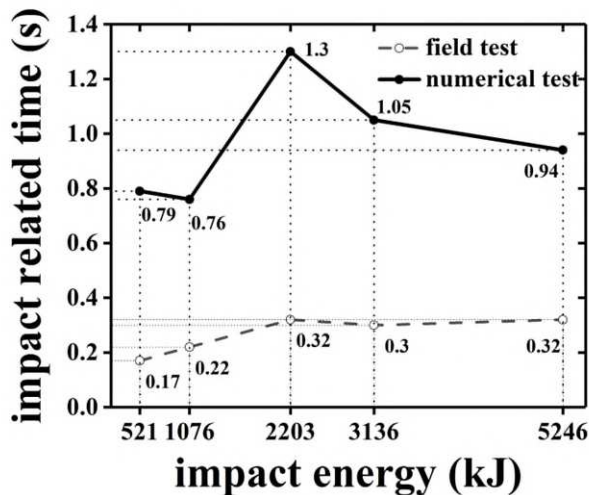
553

554 **Fig.11** Elongations of barriers versus time (left) and velocities of block versus elongation of barriers  
 555 (right)



556

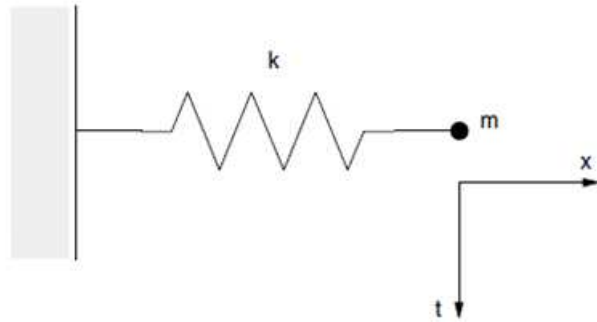
557 **Fig.12** Maximum elongation (left) and final elongation (right) versus impact energy: numerical tests  
 558 (dotted line) and field tests (solid line)



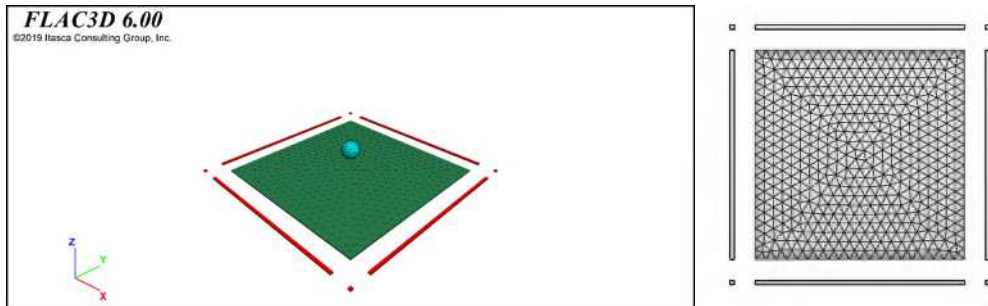
559

560 **Fig.13** Impact related time versus impact energy level: numerical tests (dotted line)  
 561 (solid line)

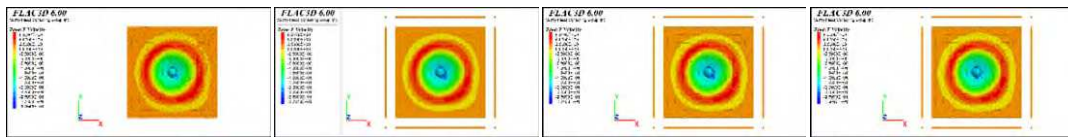
562



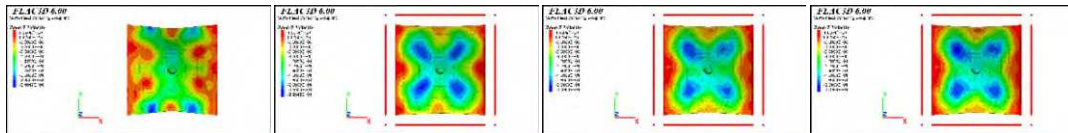
563  
564 **Fig.14** Mass- spring system in FLAC3D



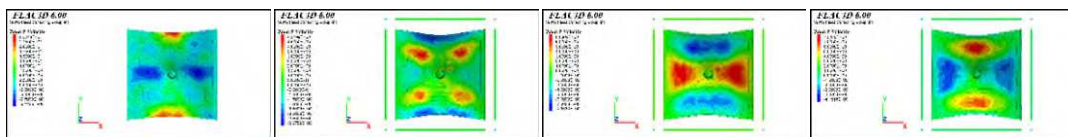
565  
566 **Fig.15** Seismic wave loading numerical model (left); topology for the mesh (right)



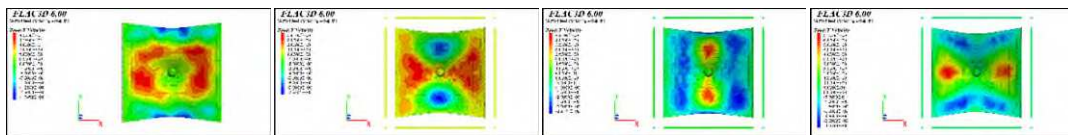
567  
568 Stage 1: contact



569  
570 Stage 2: brake



571  
572 Stage 3:

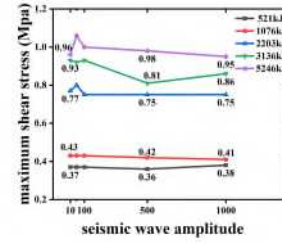
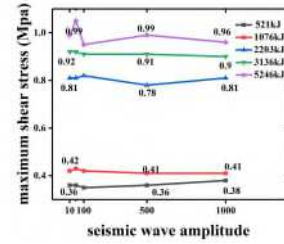
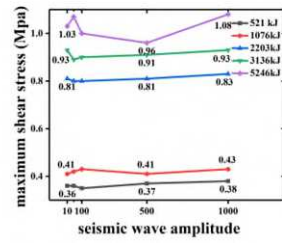
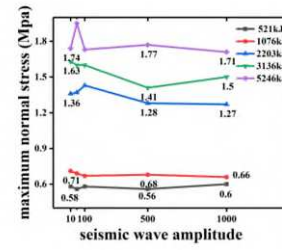
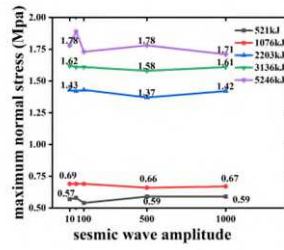
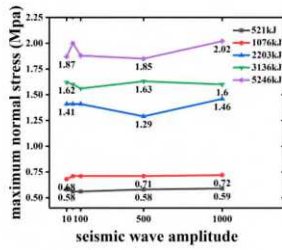


573  
574 Stage 4: rebound

575 (a) (b) (c) (d)

576 **Fig.16** Velocity contour of the barrier 500kJ rockfall impacting the protection barrier. (a) non-  
577 seismic wave (b) x-directional seismic wave, (c)y-directional seismic wave, (d) z-directional  
578 seismic wave





590

591

592

593

594

595

596

(a) (b) (c)  
**Fig.19** Maximum elongations, maximum normal stress and maximum shear stress versus seismic wave amplitude. (a)x-directional seismic wave, (b)y-directional seismic wave, (c) z-directional seismic wave